Engineering MP$_x$ (M = Fe, Co or Ni) interface electron transfer channels for boosting photocatalytic H$_2$ evolution over g-C$_3$N$_4$/MoS$_2$ layered heterojunctions

Xinyong Lu[a,b], Jun Xie[a,b], Xiaobo Chen[c,**], Xin Li[a,b,*]

[a] College of Forestry and Landscape Architecture, Key Laboratory of Energy Plants Resource and Utilization, Ministry of Agriculture, South China Agricultural University, Guangzhou, 510642, PR China
[b] College of Materials and Energy, South China Agricultural University, Guangzhou, 510642, PR China
[c] Department of Chemistry, University of Missouri – Kansas City, Kansas City, MO, 64110, USA

ARTICLE INFO

ABSTRACT

It is challenging to develop highly efficient, multifunctional and low-cost cocatalysts to accelerate transfer, separation and utilization of charge carriers for fundamentally boosting photocatalytic H$_2$ evolution. So far, the famous metallic MP$_x$ (M = Fe, Co or Ni) H$_2$-evolution cocatalyst have never been used as interface electron transfer channels between semiconductors and cocatalysts. Herein, we, for the first time, demonstrated that metal phosphide (MP) cocatalysts could be used as an interface electronic bridge to greatly enhance the photocatalytic H$_2$ evolution over 2D/2D g-C$_3$N$_4$/MoS$_2$ layered heterojunctions. The results clearly prove that Ni$_2$P could serve as much better interface electron transfer channel than CoP and Fe$_2$P. The highest hydrogen production rate of ternary g-C$_3$N$_4$-1%Ni$_2$P-1.5%MoS$_2$ could reach 532.41 μmolg^{-1}h^{-1}, which was 2.47 and 5.15 times than those of g-C$_3$N$_4$-1.5%MoS$_2$ and g-C$_3$N$_4$-1%Ni$_2$P, respectively. More importantly, the bi-functional roles of MP cocatalyts in boosting photocatalytic H$_2$ evolution were also carefully revealed. Apparently, the metallic MP cocatalysts could not only serve as normal cocatalysts to boost the H$_2$-evolution kinetics through decreasing the overpotential, but also can act as excellent interface electron transfer channels to achieve efficient transfer of more electrons from g-C$_3$N$_4$ to the surface active sites of MoS$_2$, thus synergistically leading to the significantly boosted H$_2$ evolution. This work would open up opportunities to develop high-efficiency and low-cost photocatalytic system using the rationally designed metallic earth-abundant cocatalysts as the interface electron bridge.

1. Introduction

Solar energy harnessing and conversion are the most promising routes in a great transition from the reliance of fossil fuels to the more sustainable green-energy technologies to solve energy and environmental related issues [1]. In the recent years, photocatalytic hydrogen generation over semiconductor photocatalysts from water splitting utilizing renewable solar energy has been demonstrated to be one of most eco-friendly, safe, and efficient ways to solve the energy crisis [1]. However, it is still a great challenge to fabricate high performance H$_2$-evolution photocatalysts that are earth abundant, highly efficient, low-cost, and high quantum efficiency. To date, numerous photocatalysts have been developed and well explored, including metal oxides [2,3], sulfides [4,5], and metal-free SiC [6] and graphitic carbon nitride (g-

C$_3$N$_4$) [7]. Among them, 2D g-C$_3$N$_4$ has been of great importance due to low cost, and high thermal, mechanical and chemical stability and interesting optical and electronic properties [7–9]. Intriguingly, its ideal band edge position (-1.3 V, pH = 7) and narrow bandgap (2.7 eV) have ensured the versatile applications (i.e., H$_2$ evolution and CO$_2$ photoreduction) in visible-light photocatalysis [7,9]. Even so, there still remain several disadvantages of g-C$_3$N$_4$, such as low surface area, poor conductivity and fast recombination of photo induced electron-hole pairs (with the carrier lifetime of 1 ns-100 ms), making it an inefficient photocatalyst in hydrogen evolution reaction (HER) [1]. Therefore, efforts have been devoted to improve the photocatalytic HER performance over g-C$_3$N$_4$ through different engineering modification strategies, that include element doping (metal and non-metal) [10,11], coupling with nanocarbons [12,13], construction of Type II/Z-Scheme

heterojunctions [7,14–19] and loading cocatalysts [20–22].

Particularly, loading cocatalysts has been considered as the most desire method to enhance the photocatalytic HER performance of g-C_3N_4 based photocatalysts [10]. In general, noble metals (e.g., Pt and plasmonic Au) have been used as excellent cocatalysts, due to their high activity, stability, conductivity and selectivity [23]. However, the high cost and scarcity of noble metal cocatalysts, significantly limit their practical photocatalytic applications. So it is naturally to force researchers to explore alternative earth-abundant cocatalysts [23,24]. In the past decades, many non-noble cocatalysts has emerged, such as metal phosphides [25], borides [26], carbides [27,28], and transition metal dichalcogenides (TMDs) [29,30]. Particularly, MoS_2 has attracted tremendous interest owing to its fascinating features, such as low cost, excellent HER activity, Gibbs free energy of hydrogen adsorption near to zero ($\Delta G_H \simeq 0$), graphene-like structure, semiconducting/metallic, and optical properties, capability to form hybrids/heterostructures with other materials and high chemical stability [29–31]. Thus, combining g-C_3N_4 and MoS_2 to form layered hybrids/heterostructues for diverse photocatalytic applications, particularly for H_2 evolution, has attracted much attention [32–35]. Despite the existence of synergistic effect in g-C_3N_4/MoS_2 based hybrids/heterostructures for enhancing photocatalytic HER, poor conductivity of MoS_2 and g-C_3N_4 and limited catalytic active sites of MoS_2 still seriously suppress their overall photocatalytic HER performance [34,35].

Impressively, interfacial engineering between the layered heterojunctions by coupling materials as interface electron channels for boosting HER performance is considered as an attractive and promising strategy [28,36–38]. For example, Li et al, demonstrated the improved photocatalytic performance of g-C_3N_4/NiS by coupling metallic Ni interfacial layer in the heterojuction of g-C_3N_4/NiS [37]. Similarly, Liu et al, proposed a method of incorporating CdS nanorods between the g-C_3N_4/NiS heterojunctions that showed significant enhancement in H_2 evolution [39]. However, these methods involve complex materials preparation, time-consuming process, and use of expensive reagents/chemicals. Alternatively, the transition metal phosphides (MP) (e.g. NiP_x [40,41], Co_2P [42], Cu_3P [43,44]) are a class of emerging metallic materials that are earth-abundant, low-cost and easy-synthesis. Accordingly, in theory, they could act as a potential interfacial bridge in layered hybrid heterojunction photocatalysts for boosting charge separation and enhancing photo-activity [45].

So far, to the best of our knowledge, although there are many reports describing the use of MP as cocatalysts for photocatalytic hydrogen production [46–51], the use of MP as interface electron transfer channels between the semiconductor hybrids/heterojunctions hasn't been reported. In this work, we describe the use of MoS_2 as a cocatalyst on g-C_3N_4 to design layered heterojunctions and introduce for the first time a series of MP_x (M = Fe, Co or Ni) as an interfacial electronic bridge to further boost the performance of photocatalytic H_2 evolution over MoS_2 cocatalyst.

2. Experimental section

2.1. Preparation of photocatalysts

2.1.1. Synthesis of g-C_3N_4 nanosheets

Bulk g-C_3N_4 was synthesized by following procedure described in our previous report [51]. Briefly, 30 g of urea was heated at 550 °C for 4 h with 5 °C/min to obtain yellowish bulk g-C_3N_4. Then, further heating at 500 °C for 2 h under the same condition and finally allowing cooling to room temperature yielded pale yellow bulk powders of g-C_3N_4 nanosheets.

2.1.2. Synthesis of g-C_3N_4-Ni_2P binary photocatalyst

The binary g-C_3N_4-1%Ni_2P was obtained by adopting a conventional method [52]. Approximately, 0.5 g of g-C_3N_4 was ultrasonicated in 40 mL of deionized (DI) water for 60 min to obtain colloidal dispersion. To the dispersion, 1 mL of 5 mg/mL $Ni(NO_3)_2$.6H_2O solution was added and NaOH solution (5 mg/mL) was added dropwise to the mixture with an interval of 1 h. The solution was continued stirring for 1 h. Through washing and drying, the product was annealed with NaH_2PO_2 (400 mg product corresponding to 200 mg NaH_2PO_2) in tubular furnace at 300℃ for 1 h under an inert atmosphere. Afterwards, the product was allowed to cool down to room temeperature, washed with distilled water and absolute ethanol for 3 times and dried in 60 °C for 8 h, and labeled as g-C_3N_4-1%Ni_2P. Similarly, other binary g-C_3N_4-Ni_2P samples with varying ratios were prepared by varying the volumes of Ni(NO_3)$_2$.6H_2O solution under the same experimental conditions. The pristine Ni_2P was obtained by similar step using $Ni(OH)_2$(400 mg) and NaH_2PO_2(2 g). Additionally, other MP and g-C_3N_4-MP samples were also obtained by this way.

2.1.3. Synthesis of few layers MoS_2

About 0.363g (1.5 mmol) of sodium molybdate and 0.6 g (8 mmol) of thioacetamide were dissolved in 40 mL of distilled water and kept stirring for 1 h. Then, the mixture was transferred into a Teflon lined autoclave (100 mL capacity), sealed tightly and heated at 210 °C in an air oven for 24 h. After 24 h, the autoclave was cooled to room temperature and product obtained was centrifuged, washed several times with deionised water and finally with absolute ethanol, then freeze-dried to get black powder.

2.1.4. Synthesis of ternary g-C_3N_4-Ni_2P-MoS_2 photocatalyst

0.4 g of g-C_3N_4-1%Ni_2P was taken in a plastic beaker containing 40 mL of absolute ethanol and subjected to ultrasonication for 1 h. Typically, 6 mL of MoS_2 dispersion (1 mg/mL) was slowly added to the mixture, while the mixture is kept under ultrasonication, followed by stirring for another 1 h. The obtained product after filtration was dried at 60 °C for 12 h and denoted as g-C_3N_4-1%Ni_2P-1.5%MoS_2 (as shown in Fig. 1). The other ternary photocatalysts containing different metal phosphides (Fe_2P and CoP) were also prepared under the same conditions and labeled as g-C_3N_4-1%Fe_2P-1.5%MoS_2 and g-C_3N_4-1%CoP-1.5%MoS_2, respectively.

2.2. Electrode preparation, photocatalytic H_2 evolution and electrochemical measurements

The photocatalytic H_2 production experiments by water splitting were conducted in a 100 mL Pyrex round-bottom flask. A 300 W xenon arc lamp with a UV-cutoff filter (> 400 nm) and intensity of 160 mW cm^{-2} was used as a visible light source and was positioned 19 cm away from the reactor. In a typical photocatalytic experiment, 25 mg of the as-prepared photocatalyic sample was dispersed with constant stirring in 80 mL of triethanolamine (TEOA 15 vol%) solution. Before irradiation, the suspension of the photocatalyst was dispersed in an ultrasonic bath, and nitrogen was bubbled through the reaction mixture for 30 min to ensure that the reaction system is under anaerobic conditions. After 1 h of visible light irradiation, ~0.4 mL of the evolved gas was intermittently sampled through the septum, and hydrogen was analyzed using a Gas Chromatograph (GC-7900, equipped with a thermal conductivity detector and N_2 as carrier gas).

For photoelectrocatalytic hydrogen evolution, the reactions were carried out in a standard three-electrode cell on the electrochemical workstation, using the as-synthesized samples on the glassy carbon electrode (GCE) as the working electrode, Ag/AgCl as a reference electrode and Pt plate as the counter electrode in 0.5 M H_2SO_4 electrolyte solution at the scan rate of 5mVs^{-1} for linear sweep voltammetry measuremetns. To prepare working electrodes, 6 mg of photocatalyst and 3 μL of Nafion solution (0.5%) were dispersed in 2 mL of DI water by ultrasonication for 2 h to get a homogeneous mixture. Then, 3 μL of the homogeneous mixture (containing 9 μg of the catalyst) was deposited on a glassy carbon electrode with 3 mm diameter (catalyst loading 0.03 mg cm^{-2}).
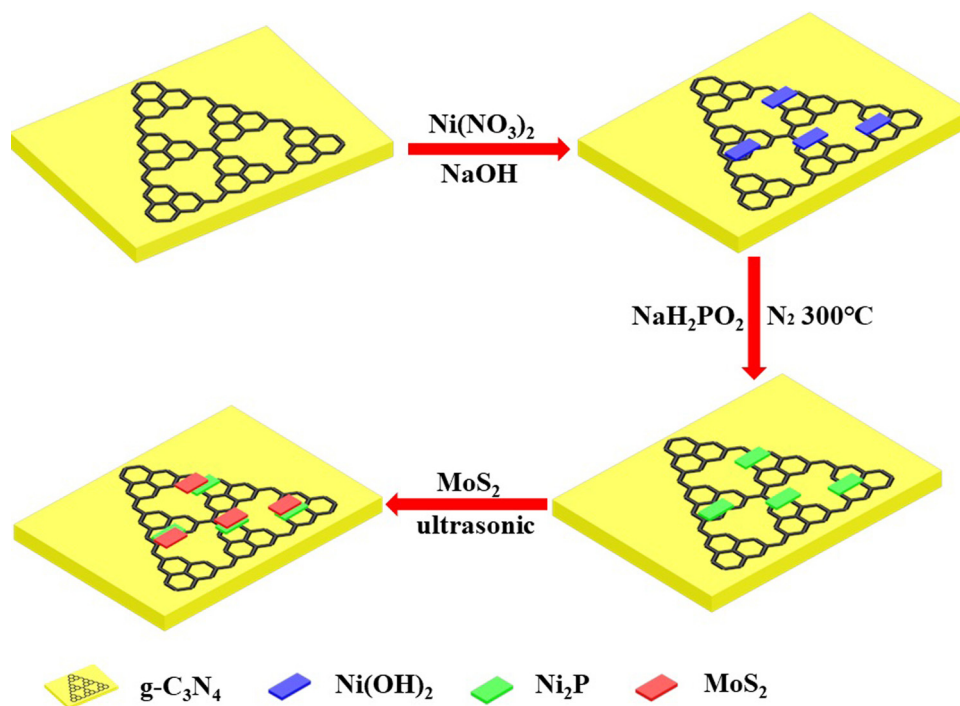
Fig. 1. Schematic illustration of the preparation of ternary g-C$_3$N$_4$/Ni$_2$P/MoS$_2$ photocatalyst.

2.3. Photoelectrochemical and transient photocurrent measurements

Transient photocurrent experiments and electrochemical impedance spectra (EIS) were performed on IM6e electrochemical workstation (Zahner Elektrik, Germany) with a standard three-electrode cell using Pt and Ag/AgCl/KCl as the counter and reference electrodes in 0.1 M Na$_2$SO$_4$ electrolyte solution. The working electrode was prepared according to the following procedure. Typically, 5 mg of photocatalyst powder was dispersed by sonication in 2 mL of ethanol containing 20 μL of 0.25% Nafion solution. Then, 0.5 mL of the solution was homogeneously spread on a FTO (2 cm × 3.5 cm) glass substrate. After coating, the FTO glasses were calcined at 150 °C for 1 h under inert atmosphere. Xe lamp (300 W) with a UV cutoff filter (λ > 420 nm) was used as the light source.

2.4. Characterization

All the synthesized samples were analyzed by recording XRD patterns using MSAL-XD2 diffractometer (Cu Kα radiation, 30 mA/36 kV, λ = 0.15406 nm). The morphology and microstructures of the samples were measured by transmission electron microscopy (TEM) and high-resolution TEM (HRTEM; JEM-2100HR 200 kV, Japan). The diffuse reflection spectra were recorded using Shimadzu UV-2550 UV–vis spectrometer equipped with the integrating sphere. The Chemical state of the as-synthesized samples were analyzed with X-ray photoelectron spectroscopy (XPS, VG ESCALAB250).The steady state photoluminescence (PL) spectra were tested on an LS50B (PerkinElmer, Inc., USA) at the excitation wavelngth of 385 nm.

3. Results and discussion

3.1. Structure, composition and optical properties

The crystal structures of the as-synthesized samples were analyzed from the powder XRD measurements. As displayed in Fig. 2A, the PXRD pattern of the synthesized MoS$_2$ sample shows the Bragg reflections at 14.5°, 33.3°, 38.4° and 41.1°, which are characteristic of 2H MoS$_2$ phase (JCPDS #17-0711) and match well with the previously reported values

[30,53,54]. While, the PXRD patterns of the metal phosphides (Ni$_2$P, CoP, and Fe$_2$P), shown in Fig. 2A, exhibit reflections marked by symbols matched well with the standard patterns of Ni$_2$P(JCPDS #89-2742), CoP(For JCPDS #89-2747), and Fe$_2$P(JCPDS #76-0089), respectively. These characteristic features match well with the previous reports [55,56]. PXRD patterns of as-synthesized g-C$_3$N$_4$ are compared with those of g-C$_3$N$_4$-MoS$_2$ hybrid and ternary g-C$_3$N$_4$-1%MP-1.5% MoS$_2$ (M-Fe, Co or Ni) in Fig. 2B. Two distinct peaks centered at 27.4° and 13.1° correspond to (200) plane of graphitic stacking and (100) in-plane tri-s-triazine repeating units, respectively (JCPDS #87-1526). These features are in good accordance with the previous reports [37,42,43,51]. The PXRD patterns of the hybrid g-C$_3$N$_4$-MoS$_2$ (Fig. 2B) show a slight increase in basal spacing compared to that of pristine g-C$_3$N$_4$, which is attributed to the random or partial intercalation of g-C$_3$N$_4$ between MoS$_2$ layers. Incorporating metal phosphides between g-C$_3$N$_4$-MoS$_2$ layers did not show any signal corresponding to metal phosphides in all the ternary samples which may be due to their low content and high dispersion on the g-C$_3$N$_4$ layers. However, further increasing the content of MP to 10%, while maintaining the amount of MoS$_2$, some MP characteristic peaks were observed (see supporting information Fig. S1). These results further suggested that the ternary samples have been successfully fabricated.

Morphology of the as-synthesized samples was analyzed from TEM and HRTEM images. Fig. 3A–C shows the TEM image of the typicalg-C$_3$N$_4$-1%Ni$_2$P-1.5%MoS$_2$ sample. The results show that the sample exhibits the folded 2D ultrathin layers with a smooth surface and high transparency, in accordance with those of the previously synthesized g-C$_3$N$_4$ [37,43,51]. Also, we have performed TEM measure for both Fe$_2$P and CoP, and their results were shown in Fig. S2. It indicates that both Fe$_2$P and CoP nanoparticles with the diameter of ~40 nm were fabricated, which expressed the obvious aggregate. As observed in Fig. 3D, the HRTEM image of g-C$_3$N$_4$-1%Ni$_2$P-1.5%MoS$_2$ shows obvious heterojunctions and distinct lattice fringes. As clearly seen in Fig. 3D, the (103) plane of MoS$_2$ with interlayer spacing of 0.219 nm can be ascribed to the crystalline 2H MoS$_2$ phase, while lattice fringe of 0.225 nm corresponds to the (111) plane of Ni$_2$P, respectively. Interestingly, an interesting phenomenon could be also found in Fig. 3D. Some indistinct interlaced lattice fringes were obviously observed,
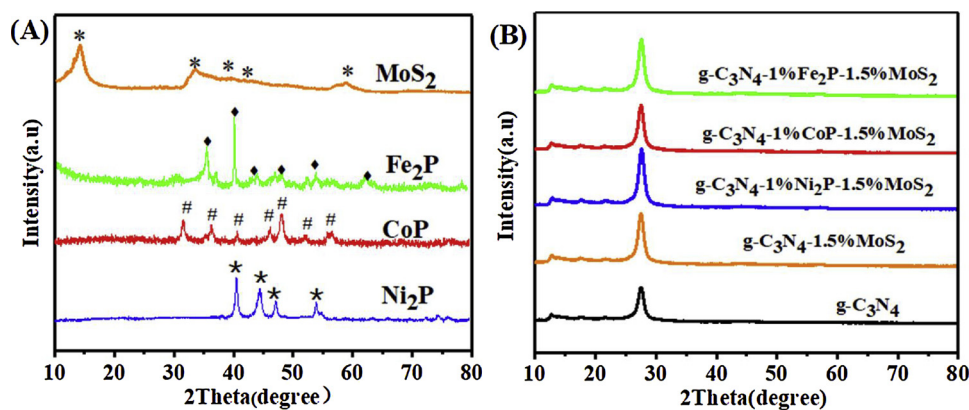
Fig. 2. (A) PXRD patterns of (a) as-synthesized MoS_2, (b) Ni_2P, (c) CoP, and (d) Fe_2P. (B) PXRD patterns of (a) as-synthesized g-C_3N_4, (b) g-C_3N_4-MoS_2, (c) g-C_3N_4-1% Ni_2P-1.5%MoS_2, (d) g-C_3N_4-1%CoP-1.5%MoS_2, and (e) g-C_3N_4-1%Fe_2P-1.5%MoS_2.

which may be ascribed to the successful coupling of Ni_2P into the interfaces between g-C_3N_4 and MoS_2. The TEM results could provide a direct evidence to confirm the successful loading of the MoS_2 nanosheets onto the surface of Ni_2P, instead of g-C_3N_4. Furthermore, EDX analysis of the same sample, as seen in Fig. 4B–G, reveals the presence and uniform distribution of the elements carbon (C), nitrogen (N), nickel (Ni), molybdenum (Mo), phosphorous (P) and sulfur (S) and no other elements were detected. Most importantly, there is relatively enough overlapping region of Ni、P、Mo and S, indicating that Ni_2P linker between g-C_3N_4 and MoS_2 has been fabricated. Based on the above results, it can be further confirmed that the metal phosphide forms an interface junction between g-C_3N_4 and MoS_2 layers.

To further ascertain the formation of ternary g-C_3N_4-1%MP-1.5%

MoS_2 (M = Fe, Co or Ni), XPS measurements were performed to identify the surface chemical composition and elemental valence states of a typical ternary g-C_3N_4-1%Ni_2P-1.5%MoS_2 photocatalyst. Fig. 5A indicates that C, N, Ni, Mo, P are actually coexisted in g-C_3N_4-1%Ni_2P-1.5%MoS_2 composites. For C 1 s spectrum (Fig. 5B), there are two distinct peaks located at 288.2 eV and 385.0 eV, corresponding to sp^2-bonded N−C = N segments and C−C group of graphitic carbon, respectively. The high-resolution N 1 s spectrum (Fig. 5C) reveals the existence of C = N−C (398.6 eV), N-C_3 (399.9 eV) and CNH (401.1 eV), while a weaker peak at 404.1 eV is assigned to π-excitation in the g-C_3N_4 substrates [37,42,43,51]. The Ni 2p spectrum in Fig. 5D show two peak located at 862.9 eV and 855.5 eV, which represent Ni $2p_{1/2}$ and Ni $2p_{3/2}$ in Ni_2P, respectively. As for P 2p spectrum (Fig. 5F) shows two
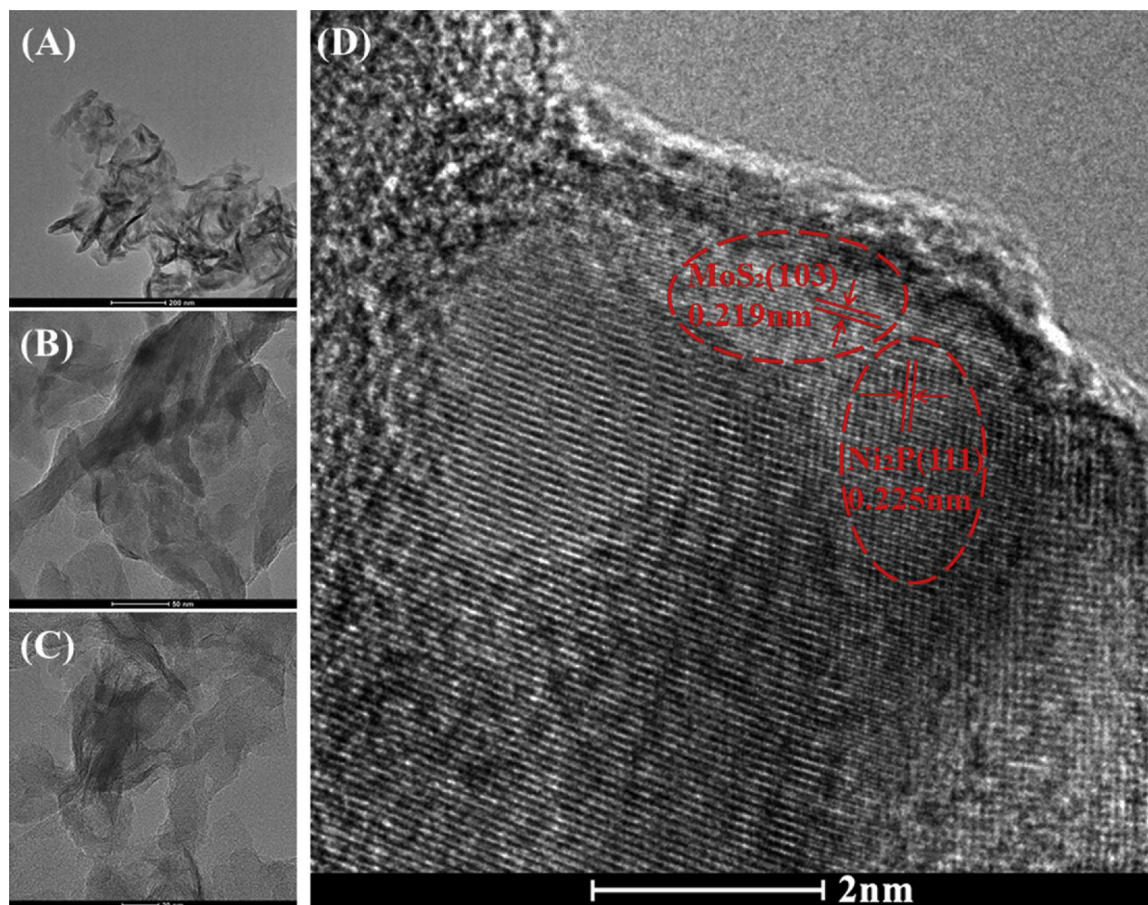

Fig. 3. TEM and HRTEM images from different regions (A–D) of g-C_3N_4-1%Ni_2P-1.5%MoS_2.
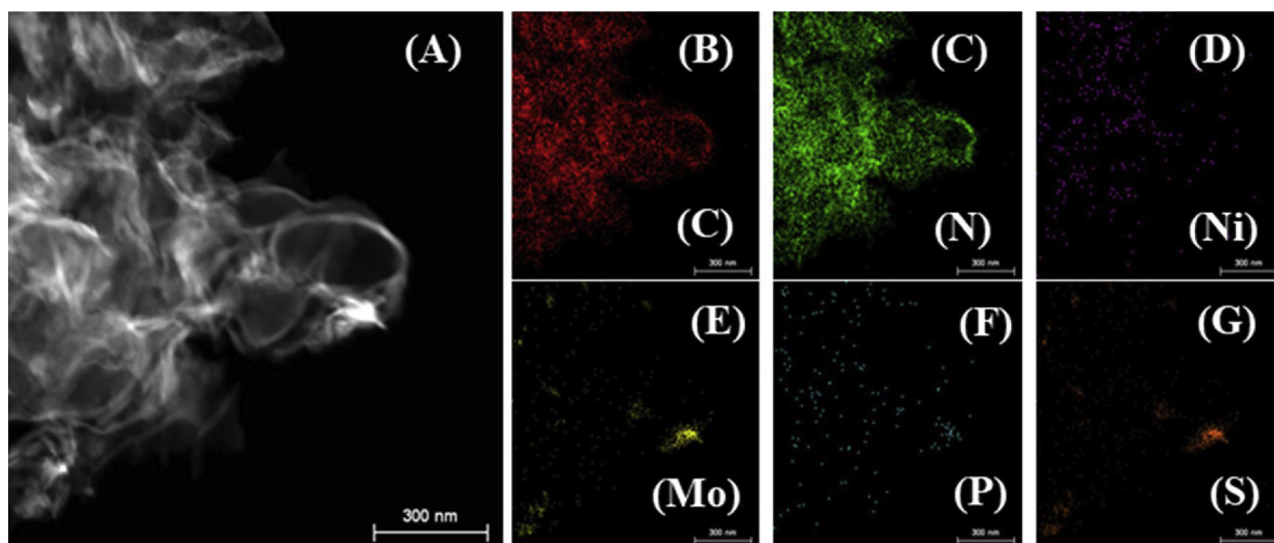
Fig. 4. EDX spectra of g-C$_3$N$_4$-1%Ni$_2$P-1.5%MoS$_2$ (A) and consisting elemental mapping of C、N、Ni、Mo、P and S.

disparate peaks. The first peak at 129.3 eV corresponds to P2p$_{3/2}$, while the stronger peak at 133.7 eV can be assigned to oxidized MP species that are arised from surface oxidation [57,58]. Clearly, the similar situation is also observed in XPS spectrum of the pure Fe$_2$P (Fig. S4) and CoP (Fig. S4).

For Fe 2p spectrum (Fig. S4A) [59], two spin-orbit doublets (707.1 eV, 719.9 eV) and (712.2 eV,725.3 eV) were clearly observed. The first one is attributed to Fe$_2$P, while the second doublet is assigned to Fe in Fe-O species caused by surface oxidation. In the XPS spectrum of P 2p (Fig. S4B), a shoulder peak at 129.8 eV, corresponding to P 2p$_{3/2}$, indicates P in phosphide state, while the peak located at 133.6 is ascribed to the PO$_x$ species. For Co 2p spectrum (Fig. S4C), two peaks around at 778.4 eV and 793.4 eV are in accordance with Co 2p$_{3/2}$ and Co 2p$_{1/2}$, while the other four peaks (781.5 eV, 785.4 eV, 797.4 eV and 802.5 eV) could be assigned to the oxidized cobalt species. The surface oxidation phenomenon was confirmed by the corresponded P 2p spectrum (Fig. S4D). The peak around at 129.7 eV means the CoP, while the peak at 133.4 eV indicate the existence of the metal oxidized phosphide when exposing air.

Based on the XPS spectrum of MP, it is indicative of not only Ni$_2$P, but also other MP, whose chemical nature and composition are well consistent with some previous reports. Also, it is worth mentioning that XPS results prove the successful formation of Ni$_2$P on g-C$_3$N$_4$ layers. For Mo3d spectrum shown in Fig. 5E reveal two major peaks of Mo3d$_{3/2}$ at 231.5 eV and Mo3d$_{5/2}$ at 228.3 eV, confirming the chemical nature of Mo^{+4}. Additionally, the S 2p spectrum (Fig. 5G) shows two peaks at 168.0 eV and162.3 eV. The stronger one could be ascribed to divalent sulfide ions (S^{2-}) for MoS$_2$ in g-C$_3$N$_4$-1%Ni$_2$P-1.5%MoS$_2$ [32,60], while the slight peak was attributed to the unexpected surface oxidation [61]. These two features of Mo3d and S2p prove the existence of 2H MoS$_2$ phase in g-C$_3$N$_4$-1%Ni$_2$P-1.5%MoS$_2$ heterojunction [32,34,35,60]. Furthermore, incorporating MP in the layered heterojunction does not produce any other defects such as Mo^{+6} in MoOS$_x$, S^{+6} or nitrogen-related defects in g-C$_3$N$_4$ as evidenced by the XPS results. Based on these results, it can be demonstrated that ternary g-C$_3$N$_4$-1%Ni$_2$P-1.5%MoS$_2$ heterojunction was prepared through a simple sonication assisted solution-based chemical route, in which MP is incorporated successfully between the layered interfaces.

In general, the photocatalytic hydrogen evolution of catalysts is mainly governed by light absorption capability and position of the band edge absorption [42]. In order to understand the light absorption capability of the samples, UV–vis diffuse reflectance spectrum was recorded for each sample. As seen in Fig. 6A, UV–vis spectra of g-C$_3$N$_4$, g-

C$_3$N$_4$-1.5%MoS$_2$ and the ternary g-C$_3$N$_4$-1%MP-1.5%MoS$_2$ (M = Fe, Co or Ni) photocatalysts exhibit almost similar absorption edge in the visible region at 445 nm, which indicated no apparent effect on the absorption edge of g-C$_3$N$_4$-1.5%MoS$_2$ after coupling MP [42,43,49]. This is in line with the similar band gap values (~2.7 eV) of the samples calculated from the Tauc plots obtained by fitting at the absorptions edge as described by the equation,

$$a = A(h\nu\text{-}E_g)^{n/2}/h\nu$$

where a, A, h, ν and E$_g$ represent absorption coefficient, proportionality constant, Planck's constant, frequency of the incident light and band energy, while n is equal to 1 due to the direct band gap transition. Despite their similar band gap values (Fig. 6B), it is interesting to note that the intensity of light absorption for the ternary g-C$_3$N$_4$-1%MP-1.5%MoS$_2$ (M = Fe, Co or Ni) photocatalysts is higher compared to those of g-C$_3$N$_4$-1.5%MoS$_2$ and pristine g-C$_3$N$_4$. This increase in absorption intensity could be attributed to incorporation of MPs (Fe$_2$P, CoP and Ni$_2$P) that enhances light absorption properties [40–43]. We believe these MPs coupled photocatalysts could be interesting for photocatalytic applications in the visible region.

3.2. Photocatalytic H$_2$ evolution activities and stabilities

In order to investigate the photocatalytic efficiency of the as-synthesized ternary layered heterojunctions, particularly how MP helps in boosting the H$_2$ evolution performance, standard photocatalytic H$_2$ evolution experiments under solar irradiation were conducted on all the samples. Fig. 7A gives the photocatalytic H$_2$ evolution activity of g-C$_3$N$_4$, g-C$_3$N$_4$-1.5%MoS$_2$ and all ternary photocatalysts, g-C$_3$N$_4$-1%-MP-1.5%MoS$_2$ (M = Fe, Co or Ni). As observed in Fig. 7A, a plot depicting amount of H$_2$ evolution *versus* time demonstrates that the H$_2$ evolution increases linearly as the time prolongs. This may be due to higher photostability for the active photocatalystsunder particular photocatalytic conditions.

Compared to pristine g-C$_3$N$_4$, amount of H$_2$ evolution for the sample g-C$_3$N$_4$-1.5%MoS$_2$ is higher which is attributed to the synergistic effect of g-C$_3$N$_4$ and MoS$_2$. Intriguingly, after coupling with MP, the average rate of H$_2$ evolution sharply increased, manifesting the key role of MP in boosting the H$_2$ evolution performance (Fig. 7B). Among all the ternary photocatlysts, the sample g-C$_3$N$_4$-1%Ni$_2$P-1.5%MoS$_2$ exhibited much higher catalytic activity towards H$_2$ evolution than CoP and Fe$_2$P-coupled photocatalysts. The increase in H$_2$-evolution rate of g-C$_3$N$_4$-1%Ni$_2$P-1.5%MoS$_2$ was almost 2.47 and 5.15 times higher than that of
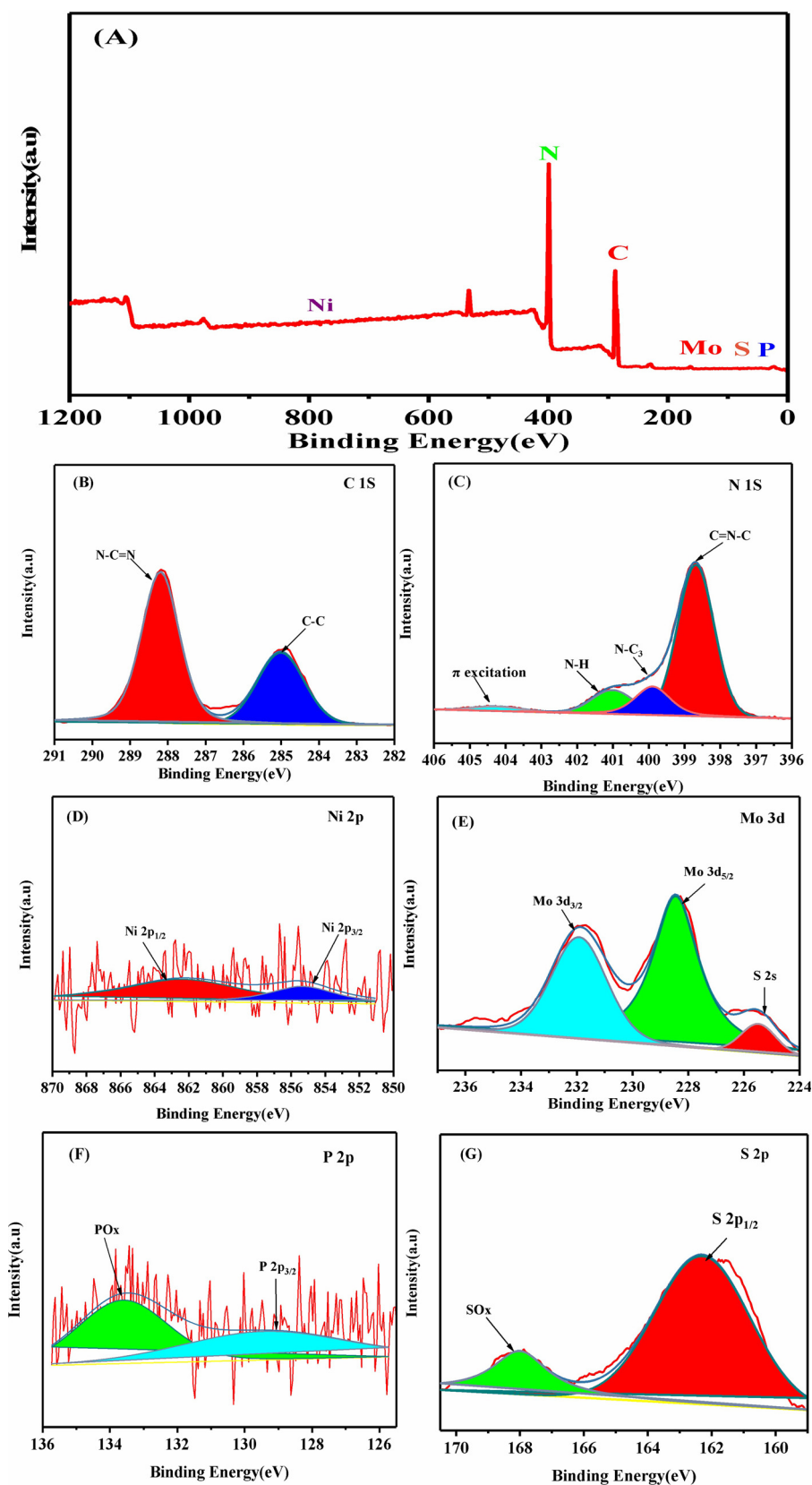
Fig. 5. XPS survey scan of (a) g-C$_3$N$_4$-1%Ni$_2$P-1.5%MoS$_2$ and corresponding core level spectra of (B) C 1s, (C) N 1s, (D) Ni 2p, (E) Mo 3d, (F) P 2p, and (G) S 2p.

individual g-C$_3$N$_4$-1.5%MoS$_2$ and g-C$_3$N$_4$-1%Ni$_2$P. Additionally, to further investigate the excellent synergistic effects in the intimate multi-heterojunctions, the photocatalytic H$_2$ evolution over the ternary physical mixture sample (simply mixing the g-C$_3$N$_4$, 1%Ni$_2$P and 1.5%

MoS$_2$) was also measured (Fig. S4). Obviously, the photocatalytic H$_2$ evolution over the sample prepared by physical mixture (Fig. S4, only 282.93 μmol g^{-1} h^{-1}), is much smaller than the sum of g-C$_3$N$_4$-1%Ni$_2$P and g-C$_3$N$_4$ -1.5%MoS$_2$ (315.64 μmol g^{-1} h^{-1}), and that of the ternary
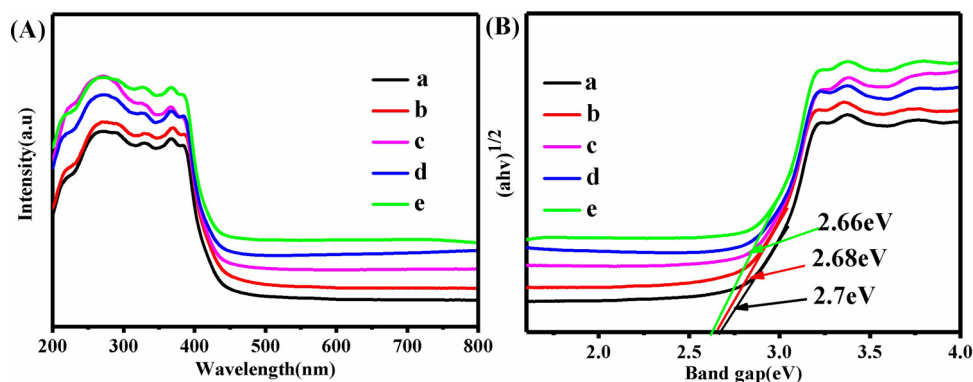
Fig. 6. (A) UV–vis diffuse reflectance spectra of (a) g-C$_3$N$_4$, (b) g-C$_3$N$_4$-1.5%MoS$_2$, (c) g-C$_3$N$_4$-1%Fe$_2$P-1.5%MoS$_2$ (d) g-C$_3$N$_4$-1%CoP-1.5%MoS$_2$ (e)g-C$_3$N$_4$-1%Ni$_2$P-1.5%MoS$_2$; (B) Tauc plots of (a) g-C$_3$N$_4$, (b) g-C$_3$N$_4$-1.5%MoS$_2$, (c) g-C$_3$N$_4$-1%Fe$_2$P-1.5%MoS$_2$ (d) g-C$_3$N$_4$-1%CoP-1.5%MoS$_2$ (e)g-C$_3$N$_4$-1%Ni$_2$P-1.5%MoS$_2$.

sample (532.41 µmol g^{-1} h^{-1}). This result indicates the enhanced performance of the ternary heterojunction photocatalyst is attributed to synergistic interactions between Ni$_2$P and MoS$_2$ cocatalysts.

The increase in photocatalytic activity of MP incorporated g-C$_3$N$_4$-1.5%MoS$_2$ may be due to the following reasons: (1) Basically, metal phosphides (MPs) have properties such as high conductivity, mechanical strength and chemical stability like other metallic structures including carbides, nitrides, borides and silicides. (2) The catalytic activity of MP is related to its crystal structure. Unlike layered metal sulphides, the large radius of P atoms (0.109 nm) in MPs tends to adopt triangular prismatic structures. This structural difference possibly

results in increase in number of coordinative unsaturated surface atoms in MPs that intrinsically show high catalytic activity [62,63]. (3) DFT studies show that rich HER activity of MPs is mainly ascribed to high electronegativity of P atoms that attracts more electrons from metal centers. Then the negatively charged P atoms act as absorption sites for H$^+$ ions, thereby boosting HER activity. (4) Furthermore, DFT studies on Ni$_2$P reveals that the exposed Ni$_2$P (001) facets show higher catalytic activity toward HER than other MP analogues [62,63]. The presence of MP at the interface could not only improve the overall conductivity and active sites but also be favorable for enhanced separation efficiency of electron-hole pairs and delayed recombination process of charge
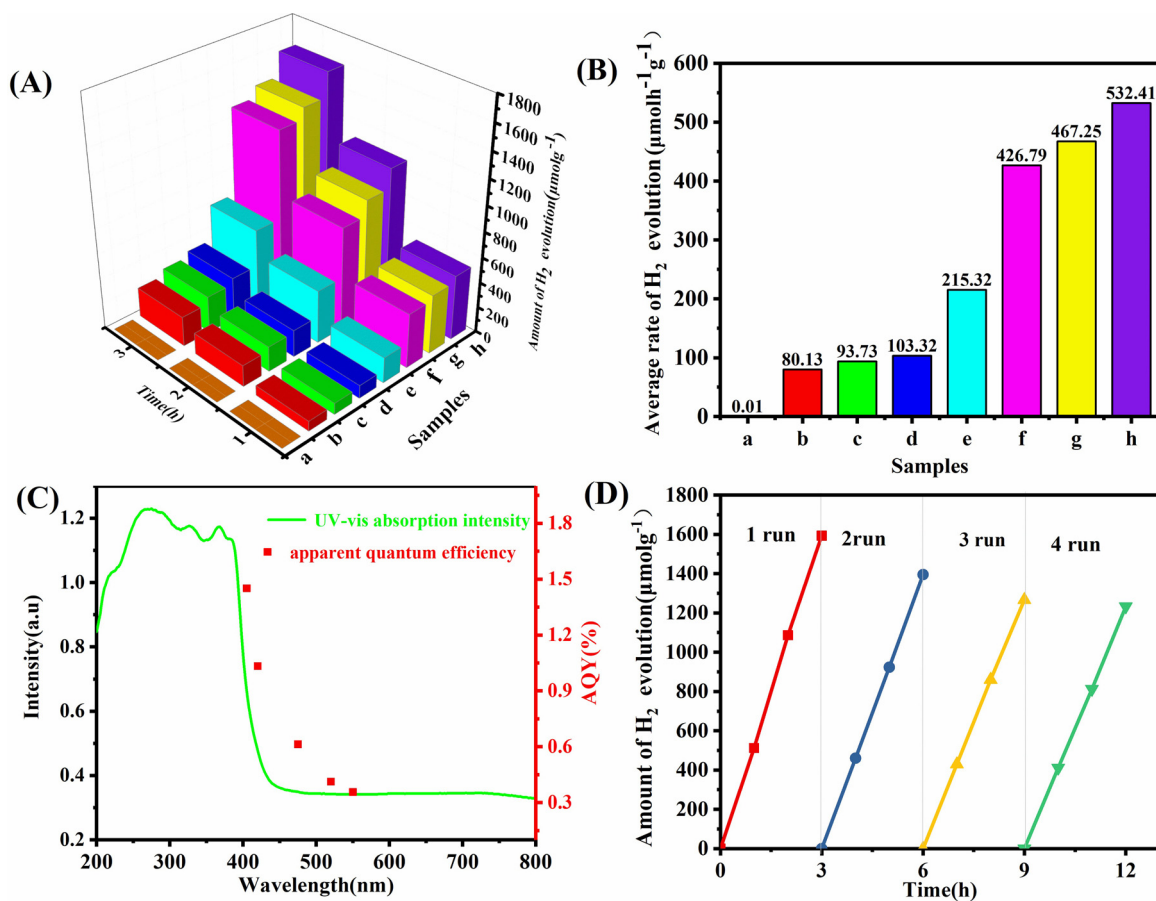

Fig. 7. (A) Time courses of photocatalytic H$_2$ evolution and (B) average photocatalytic H$_2$ production rate for different samples: (a) g-C$_3$N$_4$, (b) g-C$_3$N$_4$-1%Fe$_2$P, (c) g-C$_3$N$_4$-1%CoP,(d) g-C$_3$N$_4$-1%Ni$_2$P (e)g-C$_3$N$_4$-1.5%MoS$_2$, (f) g-C$_3$N$_4$-1%Fe$_2$P-1.5%MoS$_2$, (g) g-C$_3$N$_4$-1%CoP-1.5%MoS$_2$, (h) g-C$_3$N$_4$-1%Ni$_2$P-1.5%MoS$_2$. (C) Apparent quantum efficiency plot for g-C$_3$N$_4$-1%Ni$_2$P-1.5%MoS$_2$, (D) Stability measurements for H$_2$ gas evolution for the sample g-C$_3$N$_4$-1%Ni$_2$P-1.5%MoS$_2$ under simulated solar irradiation.

carriers. In addition, MP served as excellent electronic channels at the interface for promoting fast charge transport, thereby boosting photocatalytic H_2 production at a faster rate.

The apparent quantum efficiencies (AQEs) of ternary g-C_3N_4-1% Ni_2P-1.5%MoS_2 were further evaluated. As observed in Fig. 6C, the calculated AQE of the sample g-C_3N_4-1%Ni_2P-1.5%MoS_2 was to be 1.45% at 405 nm. AQEs of the as-prepared sample g-C_3N_4-1%Ni_2P-1.5% MoS_2 sample decrease with increasing wavelength of incident light, suggesting that the H_2 evolution depends on light absorption property of the photocatalyst. The highest AQE value matches with the absorption edge of the sample g-C_3N_4-1%Ni_2P-1.5%MoS_2, which implies that the reaction kinetics relies on absorption property.

The stability of a photocatalyst is an important factor in determining its shelf-life and efficiency. To evaluate the stability of the photocatalyst, testing cycles was performed in triethanolamine (TEOA) and result is displayed in Fig. 7D. Through four continuous cycling tests during 12 h, the sample g-C_3N_4-1%Ni_2P-1.5%MoS_2 exhibited a slight decrease (∼10-15%) in the amount of H_2 evolution but did not show any obvious degradation, suggesting its high stability for H_2 evolution in TEOA solution. During the cycle test, H_2 produced in the chamber was removed after every 3 h.

3.3. Charge separation properties

To further understand charge separation efficiency of photo-induced charge carriers, photoluminescence (PL) studies were performed with the excitation wavelength of 385 nm. Fig. 8A compares PL spectra of pristine g-C_3N_4, g-C_3N_4-1.5%MoS_2, and ternary g-C_3N_4-1%MP-1.5%

MoS_2 (M = Fe, Co or Ni). Upon comparison, pristine g-C_3N_4 and g-C_3N_4-1.5%MoS_2 show similar emission at 459 nm, while the intensity of g-C_3N_4-1.5%MoS_2 is further reduced. On the other hand, g-C_3N_4-1% MP-1.5%MoS_2 (M = Fe, Co or Ni) samples exhibit an emission at 457 nm slightly blue shifted (∼2 nm difference), while the emission intensities of PL kept drastically decreasing and the PL intensity of g-C_3N_4-1%Ni_2P-1.5%MoS_2 is the lowest. The relatively low PL intensities of g-C_3N_4-1%MP-1.5%MoS_2 (M = Fe, Co or Ni) is governed by conductive property of MPs that could be favorable to separate photogenerated charge carriers [42,43,49]. It is worthwhile to mention that a slight blue shift after MPs loading is ascribed to interaction between MPs and g-C_3N_4-1.5%MoS_2 [42,43]. It is clearly evident from the optical studies that the structure of g-C_3N_4-1%MP-1.5%MoS_2 (M = Fe, Co or Ni) could effectively separate photo-induced charge carriers, which is the key factor for improving the photocatalytic H_2 performance.

Fig. 8B demonstrates photocurrent *vs.* time curves of various electrodes that were measured under solar light radiation. The poor photoresponse of pristine g-C_3N_4 suggests poor absorption of light. For the sample g-C_3N_4-1.5%MoS_2, the photocurrent density increased to 8 μAcm^{-2}, which is attributed to coupling of MoS_2 that intensified the absorption of light. Notably, the photocurrent density of g-C_3N_4-1% Ni_2P-1.5%MoS_2 showed a value of about 3 times larger than that of g-C_3N_4-1.5%MoS_2. This may be due to the introduction of Ni_2P layers that improved the conductivity of the photocatalyst and facilitated the fast separation of photo-generated electron hole pairs, resulting in higher photocurrent density, and thereby enhanced HER activity. These observations correlate well with the UV–vis spectra (Fig. 6A) showing an increase in absorption of light as the MP layer is coupled. To further
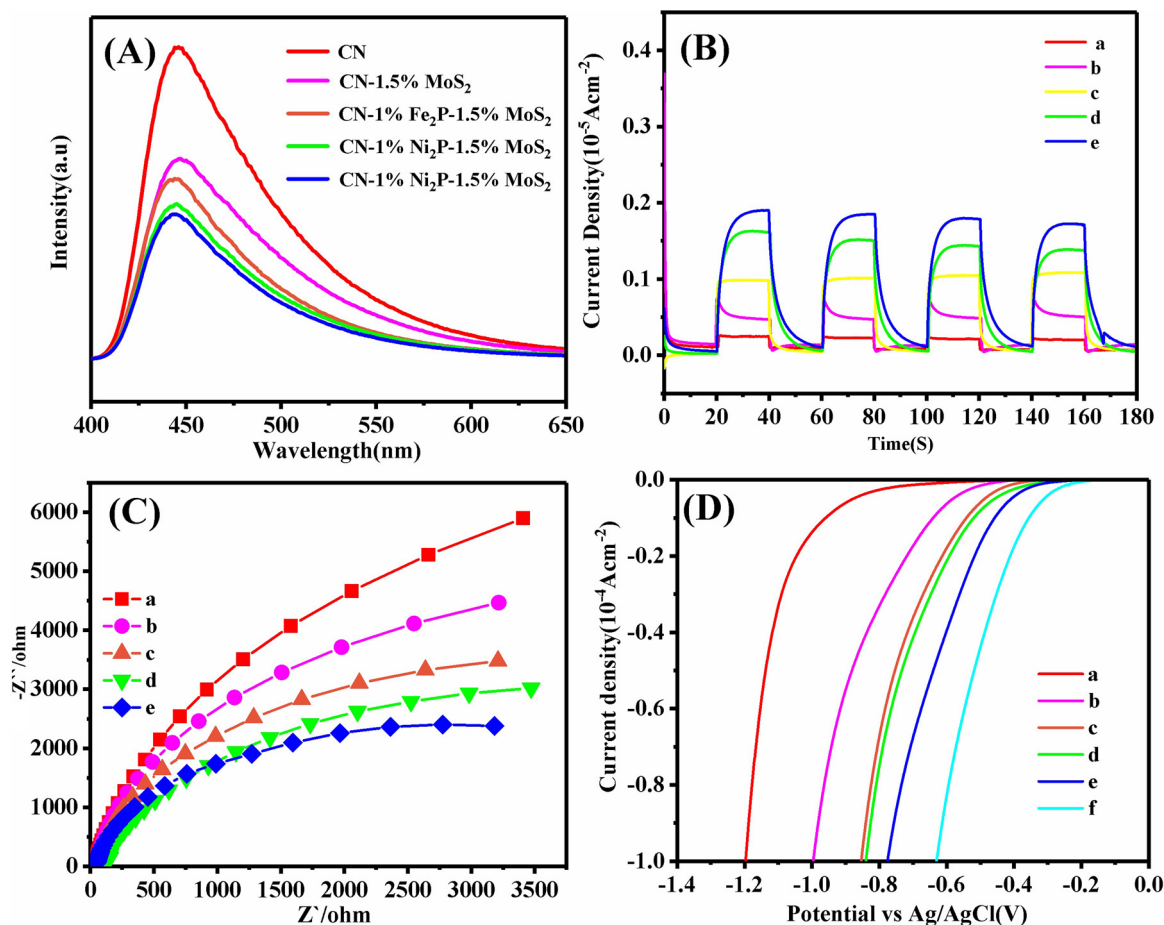

Fig. 8. (A) the PL spectra excited by irritated wavelength of 385 nm (B) Transient photocurrent responses of the as-prepared photocatalysts (C) EIS Nyquist plots and (D) the Polarization curves. Samples: (a)g-C_3N_4;(b)g-C_3N_4-1.5%MoS_2(c)g-C_3N_4-1%Fe_2P-1.5%MoS_2(d)g-C_3N_4-1%CoP-1.5%MoS_2 and (e)g-C_3N_4-1%Ni_2P-1.5%MoS_2(f) MoS_2.
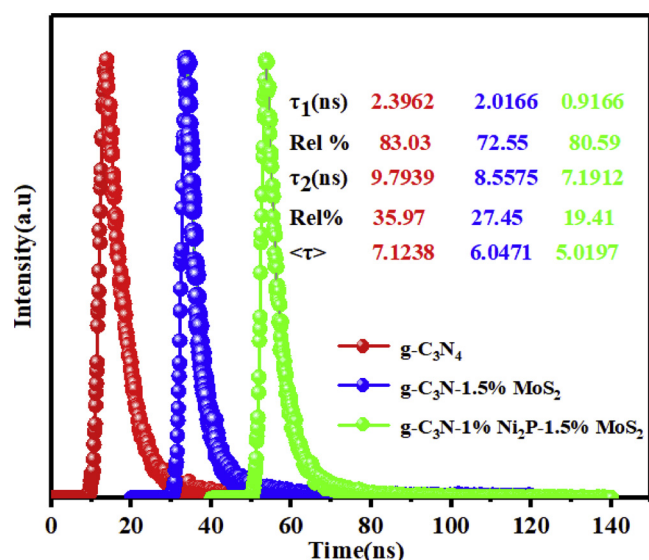
Fig. 9. Time-resolved transient PL decay of g-C$_3$N$_4$, g-C$_3$N$_4$-1.5%MoS$_2$ and g-C$_3$N$_4$-1%Ni$_2$P-1.5%MoS$_2$.

prove our perception, EIS patterns were analyzed (Fig. 8C) and found to have lower impedance for the sample g-C$_3$N$_4$-1%Ni$_2$P-1.5%MoS$_2$, corroborating the fact of enhanced conductivity and efficient electron-hole separation which contributes for high photocatalytic H$_2$ evolution [42,43].

In addition, to explore photocatalytic H$_2$ generation performance and understand the important roles of MP and MoS$_2$ played in photocatalyst. The HER polarization curves for various samples were performed and shown in Fig. 8D. As seen in the polarization curves, the g-C$_3$N$_4$-1%Ni$_2$P-1.5%MoS$_2$ electrode exhibit an much smaller overpotential than those of Fe$_2$P and CoP containing ternary samples, which is indeed much lower than pristine g-C$_3$N$_4$ and g-C$_3$N$_4$-1.5%MoS$_2$ electrode samples. This shows the excellent HER performance of g-C$_3$N$_4$-1%Ni$_2$P-1.5%MoS$_2$is attributed to enhanced conductivity by the presence of MP and fast charge transfer kinetics. Furthermore, the result coincides with the rate of photocatalytic H$_2$ evolution in Fig. 7B.

The average lifetime is an important parameter to understand the separation of charges. Time-resolved fluorescence spectroscopy was employed to investigate the importance of MP in boosting HER performance of the photocatalyst (Fig. 9).In general, more small PL average lifetime means the more desirable and effective separation of charge carrier. And this figure could be accurately calculated by the equation.

$$<\tau> = \frac{A_1\tau_1^2 + A_2\tau_2^2}{A_1\tau_1 + A_2\tau_2}$$

Where, τ_1, τ_2 represent the emission time, and A1 and A$_2$ are the corresponding amplitudes. The average lifetimes of g-C$_3$N$_4$ (7.1238 ns), g-C$_3$N$_4$-1.5%MoS$_2$ (6.0471 ns) and g-C$_3$N$_4$-1%Ni$_2$P-1.5%MoS$_2$ (5.0197 ns) were calculated individually. Additionally, the average lifetimes of g-C$_3$N$_4$-1%Fe$_2$P-1.5%MoS$_2$ and g-C$_3$N$_4$-1%CoP-1.5%MoS$_2$ were also explored by the same method, which were 5.7577 ns and 5.3797 ns (Fig. S5). This result could further prove that the Ni$_2$P, as the interface linker in g-C$_3$N$_4$-MP-MoS$_2$ system, play the better role in boosting the charge separation, compared with Fe$_2$P or CoP. Apparently, the change in average lifetime value between g-C$_3$N$_4$ and g-C$_3$N$_4$-1.5%MoS$_2$ indicates significant role of MoS$_2$ as a cocatalyst to promote charge separation.
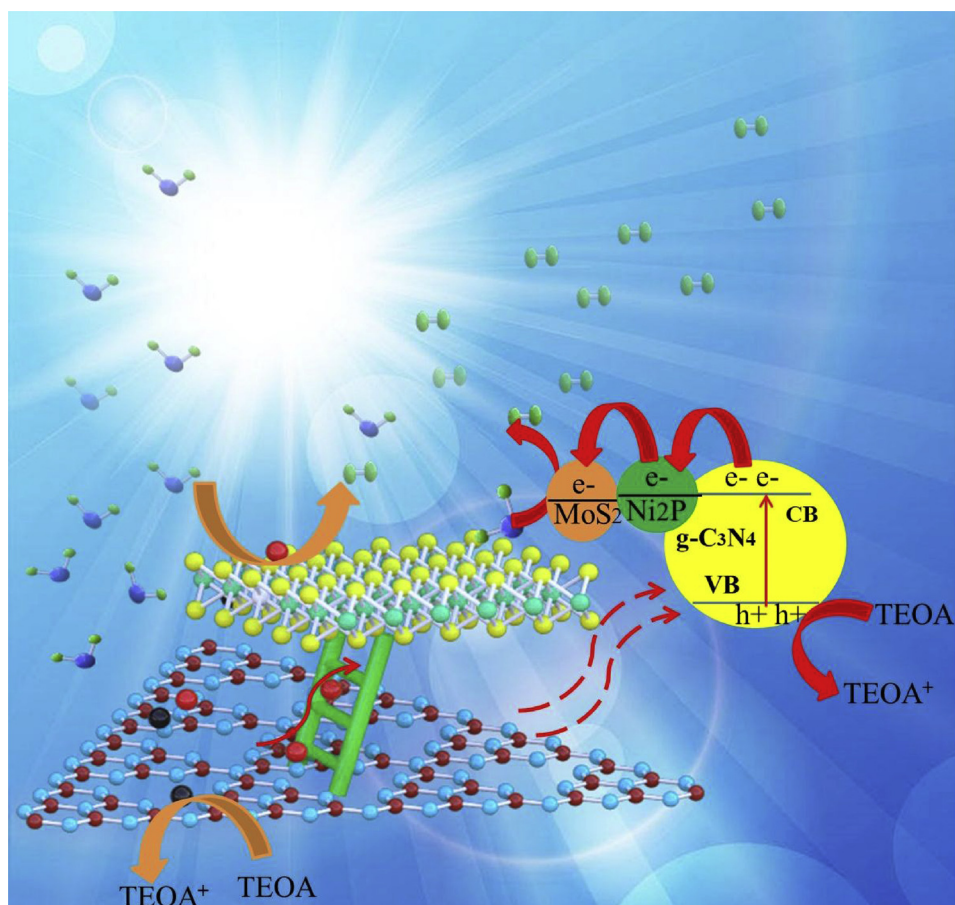

Fig. 10. Schematic representation of photocatalytic H$_2$ evolution reaction over ternary g-C$_3$N$_4$-Ni$_2$P-MoS$_2$ photocatalyst.

More importantly, after coupling Ni_2P as an interfacial channel, the smallest average lifetime (5.0197 ns) was achieved for the sample g-C_3N_4-1%Ni_2P-1.5%MoS_2, further signifying efficient charge separation that could be the reason for high HER performance.

Based on the results obtained, a probable mechanism can be speculated for ternary photocatalyst g-C_3N_4-Ni_2P-MoS_2 of visible-light driven H_2 generation and schematically shown in Fig. 10. Initially, shining visible light on g-C_3N_4 generates photo-induced electrons and hole. Subsequently, the electrons were transferred to MoS_2 layers through Ni_2P acting as interfacial electron transfer channels, thus foiling the fast recombination process of photo-generated charge carriers. The increased electrons on layered MoS_2 edges could combine with adsorbed protons, thus generating H_2 gas at a faster kinetics.

4. Conclusion

In summary, a series of MP incorporated g-C_3N_4-MoS_2 photocatalysts were synthesized by in-situ phosphorization reaction. The introduction of MP could simultaneously improve the conductivity of the photocatalyst, enahnce reactivity of active sites, promote proton adsorption kinetics and lower charge-transfer resistance. The highest HER performance (532.41 $\mu mol\,h^{-1}\,g^{-1}$) was observed for g-C_3N_4-1% Ni_2P-1.5%MoS_2. Meanwhile, other photocatalysts containing Fe_2P and CoP, also showed better photocatalytic HER activity than pristine g-C_3N_4 and binary g-C_3N_4-1.5%MoS_2 samples. Additionally, the as-prepared photocatalyst demonstrated high stability in the test cycles further confirming its photostability. Therefore, it is conclusive that the existence of MP played a pivotal role as electron transfer channels for promoting photo-induced charge separation and overall conductivity. We believe this work will provide useful insights in exploring many MP-interface photocatalysts for practical applications at large scale and resolve the problems of energy crisis.

Acknowledgements

Appendix A. Supplementary data

Supplementary material related to this article can be found, in the online version, at doi:https://doi.org/10.1016/j.apcatb.2019.04.012.

References

[1] X. Li, J. Yu, J. Low, Y. Fang, J. Xiao, X. Chen, J. Mater. Chem. A 3 (2015) 2485–2534.
[2] C.P. Sajan, S. Wageh, A.A. Al-Ghamdi, J. Yu, S. Cao, Nano Res. 9 (2016) 3–27.
[3] J. Wen, X. Li, W. Liu, Y. Fang, J. Xie, Y. Xu, Chin. J. Catal. 36 (2015) 2049–2070.
[4] Q. Li, X. Li, S. Wageh, A.A. Al-Ghamdi, J. Yu, Adv. Energy Mater. 5 (2015) 1500010.
[5] L. Cheng, Q.J. Xiang, Y.L. Liao, H.W. Zhang, Energy Environ. Sci. 11 (2018) 1362–1391.
[6] X. Zhou, Q. Gao, X. Li, Y. Liu, S. Zhang, Y. Fang, J. Li, J. Mater. Chem. A 3 (2015) 10999–11005.
[7] J. Wen, J. Xie, X. Chen, L. Xin, Appl. Surf. Sci. 391 (2017) 72–123.
[8] W.J. Ong, L.L. Tan, Y.H. Ng, S.T. Yong, S.P. Chai, Chem. Rev. 116 (2016) 7159–7329.
[9] S. Cao, J. Low, J. Yu, M. Jaroniec, Adv. Mater. 27 (2015) 2150–2176.
[10] L. Jiang, X. Yuan, Y. Pan, J. Liang, G. Zeng, Z. Wu, H. Wang, Appl. Catal. B-Environ. 217 (2017) 388–406.
[11] J. Jiang, S. Cao, C. Hu, C. Chen, Chin. J. Catal. 38 (2017) 1981–1989.
[12] X. Li, R. Shen, S. Ma, X. Chen, J. Xie, J. Appl. Surf. Sci. 430 (2018) 53–107.
[13] X. Li, J. Yu, S. Wageh, A.A. Al-Ghamdi, J. Xie, Small 12 (2016) 6640.
[14] J. Low, J. Yu, M. Jaroniec, S. Wageh, A.A. Al-Ghamdi, Adv. Mater. 29 (2017) 1601694.
[15] J. Fu, J. Yu, C. Jiang, B. Cheng, Adv. Energy Mater. (2017) 1701503.
[16] J. Low, C. Jiang, B. Cheng, S. Wageh, A.A. Al-Ghamdi, J. Yu, Small Methods 1 (2017) 1700080.
[17] Q. Xu, L. Zhang, J. Yu, S. Wageh, A.A. Al-Ghamdi, M. Jaroniec, Mater. Today 21 (2018) 1042–1063.
[18] Q. Xu, B. Zhu, C. Jiang, B. Cheng, J. Yu, Solar RRL 2 (2018) 1800006.
[19] K.L. He, J. Xie, X.Y. Luo, J.Q. Wen, S. Ma, X. Li, Y.P. Fang, X.C. Zhang, Chin. J. Catal. 38 (2017) 240–252.
[20] J. Wen, X. Li, H. Li, S. Ma, K. He, Y. Xu, Y. Fang, W. Liu, Q. Gao, Appl. Surf. Sci. 358 (2015) 204–212.
[21] M.J. Liu, P.F. Xia, L.Y. Zhang, B. Cheng, J.G. Yu, ACS Sustain. Chem. Eng. 6 (2018) 10472–10480.
[22] F. Chen, H. Yang, X.F. Wang, H.G. Yu, Chin. J. Catal. 38 (2017) 296–304.
[23] X. Li, J. Yu, M. Jaroniec, X. Chen, Chem. Rev. 119 (2019) 3962–4179.
[24] R. Shen, J. Xie, Q. Xiang, X. Chen, J. Jiang, X. Li, Chin. J. Catal. 40 (2019) 240–288.
[25] Y. Shi, B. Zhang, Chem. Soc. Rev. 45 (2016) 1781.
[26] X. Lu, J. Xie, S.-y. Liu, A. Adamski, X. Chen, X. Li, ACS Sustain. Chem. Eng. 6 (2018) 13140–13150.
[27] S. Ma, Y.P. Deng, J. Xie, K.L. He, W. Liu, X.B. Chen, X. Li, Appl. Catal. B-Environ. 227 (2018) 218–228.
[28] K. He, J. Xie, Z.Q. Liu, N. Li, X. Chen, J. Hu, X. Li, J. Mater. Chem. A 6 (2018) 13110–13122.
[29] A.A. Jeffery, S.R. Rao, M. Rajamathi, Carbon 112 (2017) 8–16.
[30] S. Ma, J. Xie, J. Wen, K. He, X. Li, W. Liu, X. Zhang, Appl. Surf. Sci. 391 (2017) 580–591.
[31] M. Chhowalla, H.S. Shin, G. Eda, L.J. Li, K.P. Loh, Z. Hua, Nat. Chem. 5 (2013) 263–275.
[32] L. Ge, C.C. Han, X.L. Xiao, L.L. Guo, Int. J. Hydrogen. Energy 38 (2013) 6960–6969.
[33] H. Zhao, Y.M. Dong, P.P. Jiang, H.Y. Miao, G.L. Wang, J.J. Zhang, J. Mater. Chem. A 3 (2015) 7375–7381.
[34] N. Li, J. Zhou, Z.Q. Sheng, W. Xiao, Appl. Surf. Sci. 430 (2018) 218–224.
[35] X.W. Shi, M. Fujitsuka, S. Kim, T. Majima, Small 14 (2018) e1703277.
[36] Y. Yuan, W. Li, Y. Tong, L. Gu, Z.M. Xue, Sustain Energy Fuels 2 (2018) 2502–2506.
[37] J.Q. Wen, J. Xie, H.D. Zhang, A.P. Zhang, Y.J. Liu, X.B. Chen, X. Li, ACS Appl. Mater. Interfaces 9 (2017) 14031–14042.
[38] R. Shen, W. Liu, D. Ren, J. Xie, X. Li, Appl. Surf. Sci. 466 (2019) 393–400.
[39] J. Yuan, J. Wen, Y. Zhong, X. Li, Y. Fang, S. Zhang, W. Liu, J. Mater. Chem. A 3 (2015) 18244–18255.
[40] J. Wen, J. Xie, R. Shen, X. Li, X. Luo, H. Zhang, A. Zhang, G. Bi, Dalton Trans. 46 (2017) 1794–1802.
[41] D. Zeng, W. Xu, W.-J. Ong, J. Xu, H. Ren, Y. Chen, H. Zheng, D.-L. Peng, Appl. Catal. B-Environ. 221 (2018) 47–55.
[42] R.C. Shen, J. Xie, H.D. Zhang, A.P. Zhang, X.B. Chen, X. Li, ACS Sustain. Chem. Eng. 6 (2018) 816–826.
[43] R.C. Shen, J. Xie, X.Y. Lu, X.B. Chen, X. Li, ACS Sustain. Chem. Eng. 6 (2018) 4026–4036.
[44] R. Shen, J. Xie, Y. Ding, S.-y. Liu, A. Adamski, X. Chen, X. Li, ACS Sustain. Chem. Eng. 7 (2019) 3243–3250.
[45] W. Yang, B. Kong, D. Zhao, H. Wang, C. Selomulya, Nano Today 15 (2017) 26–55.
[46] X.-l. Li, X.-j. Wang, J.-y. Zhu, Y.-p. Li, J. Zhao, F.-t. Li, Chem. Eng. J. 353 (2018) 15–24.
[47] D. Dai, X. Hao, G. Lei, C. Han, Y. Gao, S. Li, L. Yan, Appl. Catal. B-Environ. 217 (2017) 429–436.
[48] D. Dai, L. Wang, N. Xiao, S. Li, H. Xu, S. Liu, B. Xu, D. Lv, Y. Gao, W. Song, L. Ge, J. Liu, Appl. Catal. B-Environ. 233 (2018) 194–201.
[49] J. Xu, Y. Qi, C. Wang, L. Wang, Appl. Catal. B-Environ. 241 (2019) 178–186.
[50] T. Di, B. Zhu, J. Zhang, C. Bei, J. Yu, Appl. Surf. Sci. 389 (2016) 775–782.
[51] G. Bi, J. Wen, X. Li, W. Liu, J. Xie, Y. Fang, W. Zhang, RSC Adv. 6 (2016) 31497–31506.
[52] H. Zhao, J.W. Wang, Y.M. Dong, P.P. Jiang, ACS Sustain. Chem. Eng. 5 (2017) 8053–8060.
[53] X. Qian, J. Ding, J. Zhang, Y. Zhang, Y. Wang, E. Kan, X. Wang, J. Zhu, Nanoscale 10 (2018) 1766–1773.
[54] K.J. Huang, J.Z. Zhang, G.W. Shi, Y.M. Liu, Electrochim. Acta 132 (2014) 397–403.
[55] L. Feng, H. Vrubel, M. Bensimon, X. Hu, Phys. Chem. Chem. Phys. 16 (2014) 5917–5921.
[56] E.J. Popczun, C.W. Roske, C.G. Read, J.C. Crompton, J.M. McEnaney, J.F. Callejas, N.S. Lewis, R.E. Schaak, J. Mater. Chem. A 3 (2015) 5420–5425.
[57] Z. Xing, Q. Liu, A.M. Asiri, X. Sun, Adv. Mater. 26 (2014) 5702–5707.
[58] Y.-Y. Ma, C.-X. Wu, X.-J. Feng, H.-Q. Tan, L.-K. Yan, Y. Liu, Z.-H. Kang, E.-B. Wang, Y.-G. Li, Energy Environ. Sci. 10 (2017) 788–798.
[59] X. Zhang, X. Zhang, H. Xu, Z. Wu, H. Wang, Y. Liang, Adv. Funct. Mater. 27 (2017) 1606635.
[60] J. Li, E.Z. Liu, Y.N. Ma, X.Y. Hu, J. Wan, L. Sun, J. Fan, Appl. Surf. Sci. 364 (2016) 694–702.
[61] L. Cai, J. He, Q. Liu, T. Yao, L. Chen, W. Yan, F. Hu, Y. Jiang, Y. Zhao, T. Hu, Z. Sun, S. Wei, J. Am. Chem. Soc. 137 (2015) 2622–2627.
[62] Y.M. Shi, B. Zhang, Chem. Soc. Rev. 45 (2016) 1529–1541.
[63] P. Liu, J.A. Rodriguez, J. Am. Chem. Soc. 127 (2005) 14871–14878.